scRNAseq comparison of healthy and irradiated mouse parotid glands highlights immune involvement during chronic gland dysfunction

Brenna Rheinheimer[2], Mary C. Pasquale[1], GCBC[3], Kirsten H. Limesand[2], Matthew P. Hoffman[1], Alejandro M Chibly[1*]

[1]Matrix and Morphogenesis Section, National Institute of Dental and Craniofacial Research, National Institutes of Health, Bethesda, MD 20892.

[2]Nutritional Sciences Department, University of Arizona, Tucson, AZ. 85721

[3]Genomics and Computational Biology Core, National Institute of Dental and Craniofacial Research, National Institutes of Health, Bethesda, MD 20892. USA.

Running title. Single cell RNAseq analysis of parotid glands

Key words. scRNAseq, salivary gland, parotid, PG, irradiation

*Corresponding author:
Alejandro M. Chibly
Matrix and Morphogenesis Section, NIDCR, NIH, Bethesda, MD 20892, USA
Email: martinez-chibly.agustin@gene.com
Current address: Reverse Translation, Oncology Bioinformatics, Genentech, Inc. 1 DNA Way, South San Francisco, CA. 94080

HIGHLIGHTS

- We generated a scRNAseq dataset of chronic post-irradiation injury in parotid glands
- A newly identified *Etv1*+ epithelial population may be acinar precursors
- Ntrk2 and Erbb3 are highly specific Etv1+ cell receptors that may mediate cell-cell communication with myoepithelial cells
- CD8+ T-cells and secretory acinar cells have the greatest transcriptional changes post-IR

SUMMARY

Translational frameworks to understand the chronic loss of salivary dysfunction that follows after clinical irradiation, and the development of regenerative therapies remain an unmet clinical need. Understanding the transcriptional landscape long after irradiation treatment that results in chronic salivary hypofunction will help identify injury mechanisms and develop regenerative therapies to address this need. Advances in single cell (sc)RNAseq have made it possible to identify previously uncharacterized cell types within tissues and to uncover gene regulatory networks that mediate cell-cell communication and drive specific cell states. scRNAseq studies have been performed for virtually all major tissues including salivary glands; however, there are currently no scRNAseq studies the long-term chronic effects of irradiation on salivary glands. Here, we present scRNAseq from control and irradiated murine parotid glands collected 10 months post-irradiation. We identify a previously uncharacterized population of epithelial cells in the gland defined by expression of *Etv1*, which may be an acinar cell precursor. These Etv1+ cells also express *Ntrk2* and *Erbb3* and thus may respond to myoepithelial cell-derived growth factor ligands. Furthermore, our data suggests that CD8+ T-cells and secretory cells are the most transcriptionally affected during chronic injury with radiation, suggesting active immune involvement during chronic injury post-irradiation. Thus, our study provides a resource to understand the transcriptional landscape in a chronic post-irradiation microenvironment and identifies cell-specific pathways that may be targeted to repair chronic damage.

Introduction

Of the three major pairs of salivary glands (SGs): the parotid (PG), submandibular (SMG), and sublingual (SLG), the PG produces the largest volume of saliva, particularly in response to gustatory simulation. In addition, the PG is the most sensitive to irradiation (IR) damage, a therapeutic treatment for head and neck cancer that often results in permanent salivary hypofunction. In terms of understanding salivary gland biology, most studies have focused on the SMG both in the context of development and response to injury; however, each gland has unique functions and transcriptional profile (Gao et al., 2018). Here we set out to investigate the effects of irradiation damage to PGs in mice using single cell (sc)RNAseq.

The PG is primarily comprised of serous acinar cells which produce large volumes of watery serous saliva that is transported through the ductal system into the oral cavity to aid in digestion and protection of mucosal surfaces. Despite advances in tumor tissue targeting during radiotherapy, it is estimated that > 73% of head and neck cancer patients suffer from the chronic consequences of salivary gland damage months to years after the completion of radiotherapy (Jensen et al., 2010). Animal studies show that the acute effects of radiotherapy in the PG occur in the days and weeks following initial treatment and are likely a result of high levels of acinar cell death (Eisbruch et al., 1999; Grundmann et al., 2009; Henson et al., 1999; Robar et al., 2007), whereas the chronic effects arise months to years after initial treatment. Chronic loss of function is often attributed to fibrosis and the inability of acinar regeneration to occur, and preclinical studies suggest that persistent acinar cell proliferation, vascular damage, and parenchymal cell loss may be contributing factors (Dirix et al., 2006; Grundmann *et al.*, 2009; Li et al., 2007; Radfar and Sirois, 2003). In a similar manner, patients with Sjogren's syndrome, an autoimmune disease that damages the acinar cells of salivary and lacrimal glands, life-long consequences include dental caries, reduced taste and smell, malnutrition, mucositis, and increased risk for oral infections leading to a significant decrease in quality of life (Vissink et al., 2010). Therefore, translational frameworks to understand chronic glandular dysfunction following IR therapy along with the development of regenerative therapies remains an unmet need.

The development of scRNAseq has made it possible to identify previously uncharacterized cell types within a tissue and to uncover and gene regulatory networks and mechanisms regulating cell-cell communication and specific cell states (Grün and van Oudenaarden, 2015; Kolodziejczyk et al., 2015; Trapnell, 2015; Wang and Navin, 2015). To date, there have been scRNAseq studies performed for virtually all major tissues, including atlas-level scRNAseq datasets such as the

Tabula Muris (Tabula Muris et al., 2018) or the Tabula Sapiens (Tabula Sapiens et al., 2022) which integrate data from multiple organs in mouse and human, respectively. There are also numerous scRNAseq studies on disease-specific models, which are important to understand the cellular mechanisms involved that could be targeted for repair or regeneration. In SGs, scRNAseq studies have focused on either homeostasis or development (Chen et al., 2022; Hauser et al., 2020; Huang et al., 2021; Oyelakin et al., 2019; Sekiguchi et al., 2020), but not on injury or disease models.

In this study, we use scRNAseq analysis to characterize the adult mouse PG and compare the transcriptional landscape 10 months after IR damage as a model to explore chronic dysfunction post-irradiation. The model of SG IR used in this study recapitulates the loss of function observed in humans and has been instrumental in evaluating the therapeutic potential of adenovirus-associated neurturin-gene transfer (Ferreira et al., 2018). Thus, investigation of cell-type-specific gene expression in this model will be a valuable resource to understand the molecular mechanisms underlying health and disease in SGs. Due to the complex heterogeneity of the SGs, distinguishing cell-type compositional differences and their specific and direct contribution to the loss of saliva following radiation therapy is complex, and single-cell transcriptomics will begin to resolve this issue.

This dataset allows for discovery and exploratory research into the mechanisms and cellular processes driving PG dysfunction post-IR. Our work has been validated by immunofluorescence staining to confirm the presence of selected markers in specific cell populations, confirming the potential to reveal meaningful biological insights. It is noteworthy that scRNAseq of in vivo models of chronic IR injury has only been performed in liver (Xu et al., 2021), lung (Mukherjee et al., 2021), and skin (Paldor et al., 2022), and data is only publicly available for lung and skin. Thus, our study will also be an essential resource to better understand cell-specific responses to IR in general.

Results

Generation of a single-cell resource of healthy and irradiated mouse parotid gland

Using the 10X Genomics platform, we generated 2 individual scRNAseq libraries of healthy and IR mouse PG collected 10-months post-irradiation (Figure 1A). Mice received 5 Gy IR/day to the head and neck region on six consecutive days, for a total dose of 30 Gy. This mouse model of IR damage to SGs results in chronic loss of saliva with partial loss of epithelial cells

(Teos et al., 2016). Control and IR PG samples were bioinformatically integrated with SEURAT v3 and clustered following SEURAT's standard workflow (Stuart et al., 2019). The optimal resolution for clustering was determined using clustree package (Zappia and Oshlack, 2018) and the resulting 17 cell clusters were annotated based on their gene expression profile (Figure 1B, S1A-B) and a previously generated atlas of SMG development which provided cell type specific markers (Hauser *et al.*, 2020). Stromal and myoepithelial cells clustered together with endothelial cells likely due to the low number of cells recovered for these populations. Thus, they were manually annotated based on expression of a combination of stromal (*Col1a12* and *Vim*) and myoepithelial (*Krt14* and *Acta2*) markers which were highly specific (Figure S1C-D). We did not identify discrete clusters of basal duct cells (*Krt14*+*Krt5*+) or peripheral nerves presumably due to limitations in the dissociation technique, which has been previously reported for adult SG tissue dissociation.

The identified populations included acinar cells (*Amy1*+), intercalated duct (*Dcpp1-3*+), striated duct (*Fxyd2*+, *Klk1*+), myoepithelial cells (*Acta2*+*Krt14*+), stromal (*Col1a1*+*Vim*+), endothelial (*Pecam1*+), and 9 distinct immune populations including B-cells (*Cd79a*+ and Immunoglobulin genes), five subtypes of T-cells (*CD4*+; *CD8*+; *CD4*+*CD8*+; *FoxP3*+; *Cxcr6*+), macrophages (*Adgre1*+), dendritic cells (*S100a8/9*+), and natural killer cells (*Gzma*+*Nkg7*+). We also identified a previously uncharacterized epithelial population defined by high expression of *Etv1* and *Krt8* and moderate expression of *Amy1* (Figure 1B-C, S1B).

Etv1 delineates an epithelial subpopulation, similar to SMG IDs that is involved in Rap1, TNF, and ErbB signaling

The two most striking observations from our initial clustering analysis are the identification of an *Etv1*+ epithelial population and the prominence of multiple resident immune cell types after IR. *Etv1* is associated with embryonic development of the acinar epithelium in mouse SMG and its expression correlated with that of the acinar gene *Bhlha15*/Mist1 (Hauser *et al.*, 2020) but it did not define a unique population in adult SMGs. In the developing SMG, *Etv1* is more highly expressed in end bud cells compared to ducts at E13 and increases in expression at E16 when proacinar differentiation begins (data from SGMAP, add Hauser et al, 2020). To characterize this *Etv1*+ cluster, and to generate gene expression profiles of individual cell populations in healthy adult parotid glands, we performed differential expression analysis with SEURAT in the annotated

control sample (Figure 1C). Genes enriched in a given cluster are herein referred to as cell-defining genes and were sometimes expressed elsewhere at lower levels. The complete gene list is included in Supplementary File 1.

The expression of Amy1 in *Etv1*+ cells suggested an acinar-like phenotype. When comparing the gene expression profile of major epithelial populations, 38% of acinar-defining genes (30 of 79) were enriched in *Etv1*+ cells (Figure 2A-B). Both cell types expressed serous secretory markers such as amylase (*Amy1*), parotid secretory protein (*Bpifa2*), prolactin induced protein (*Pip*), and carbonic anhydrase 6 (*Car6*), but their expression was significantly higher in acinar cells, while *Etv1*+ cells had higher expression of *Krt8, Krt18,* and *Phlda1* (Figure 2C). When compared to duct populations, *Etv1*+ cells expressed 38% (19 genes) of intercalated duct (ID)-defining genes (Figure S2A) and only 9.3% of striated duct (SD)-defining genes (Figure 2B, S2B), suggesting that *Etv1*+ cells are transcriptionally similar to both acinar and ID populations. Accordingly, Etv1 protein was detected by immunofluorescence in a subset of duct and acinar cells. Duct cells showed strong nuclear and cytoplasmic Etv1+ signal while it was predominantly nuclear in NKCC1+ acinar cells (Figure 2D).

Next, we performed functional analysis of all acinar and *Etv1*+ cell-defining genes using STITCH (search tool for interactions of chemicals, http://stitch.embl.de/), which integrates information about interactions from metabolic and KEGG pathways, crystal structures, binding experiments, and drug-target relationships. (Kuhn et al., 2008). As expected, KEGG pathway analysis on acinar genes showed salivary secretion as one of the top pathways (Figure S2D). In contrast, in *Etv1*+ cells the top functions and pathways were associated with organ development and activation of Rap1, TNF, and ErbB signaling pathways (Figure 2E, S2C), suggesting that the *Etv1*+ population has distinct functions despite their transcriptional similarities to acinar cells.

Computational analysis reveals potential interactions between myoepithelial cells, acinar, and Etv1+ cells via Erbb3 and Ntrk2 receptors

Given that cellular functions are often initiated by ligand-receptor interactions that trigger signaling cascades, we next evaluated the presence of known ligands and receptors among the cell-defining genes for each population and used this information to predict putative cell-cell interactions. Ligand and receptor genes were identified based on a previously published database of curated ligand-receptor pairs (Ramilowski et al., 2015). In this database, a ligand is defined as

any molecule that interacts with known receptors and intracellular components such as *Hras* are included. Acinar and duct cells had the lowest number of enriched ligand and receptor genes compared to all other cell types while myoepithelial cells had the highest number across epithelial populations (Figure S3A-B). Nonetheless, we identified 9 ligand and 5 receptor genes among the *Etv1*+ cell-defining genes, as well as 5 ligands and 2 receptors in acinar cells (Figure 3A). The identified receptor genes enriched in *Etv1*+ cells included *Ghr*, *Dddr1*, *St14*, *Erbb3,* and *Epha5*, which were highly specific to this population (Figure 3B, left panel). On the other hand, the ligands found in *Etv1*+ cells were also enriched in other cell types, with the exception of *Col7a1,* which was highly specific (Figure 3B, right panel). A distinct set of ligands and receptors were enriched in acinar cells, including the receptor genes *Ntrk2* and *Kcnn4*, and the ligands *P4hb, Nucb2, Agt, Tcn2,* and *Pip.*

In order to automate the prediction of potential ligand-receptor interactions in a reproducible way, we used R scripted code to leverage the genes identified in our scRNAseq dataset against the database of ligand-receptor pairs (Ramilowski *et al.*, 2015). The source code is available as supplementary material. The resulting putative interactions between acinar and *Etv1*+ cells with all other cell types are shown in Tables 1 and 2 and summarized as chord plots in Figure 3D-E. All remaining putative interactions are available in supplementary file 2. Based simply on the total number of possible pairs (without accounting for the level of expression of individual genes), the strongest outgoing interactions from *Etv1*+ cell ligands were predicted to occur with receptors in endothelial cells, whereas *Etv1*+ cell receptors could primarily interact with ligands from myoepithelial and stromal cells (Figure 3D-E). Notably, a putative myoepithelial-*Etv1*+ cell interaction was predicted via the *Erbb3* receptor and two of its ligands, Neuregulin1 (*Nrg1*) and *Nrg2* (Figure 3E).

A putative myoepithelial-acinar interaction was also predicted to occur via the neurotrophin receptor *Ntrk2* and one of its ligands, Neurotrophin 3 (*Ntf3*). *Ntrk2* was also expressed in *Etv1*+, myoepithelial and stromal cells in our scRNAseq data but immunofluorescence staining confirmed enrichment of the receptor in acinar cells of mouse parotid gland (Figure 3F). The cellular functions of *Ntrk2* in acinar cells are currently unknown and thus further mechanistic studies are warranted.

CD8+CD4+ T-cells and acinar cells have the greatest transcriptional response to IR

The combined damage to the SG parenchyma and its microenvironment is proposed to be responsible for the lack of regeneration and subsequent loss of saliva that result from IR injury. Understanding how specific cell populations are affected by IR will inform future mechanistic studies for the development of cell-based regenerative therapies. Thus, our next goal was to characterize the cell-specific responses to chronic IR damage, both in terms of cell proportions and transcriptional profile. Given that we did not perform multiple technical replicates of each treatment, potential changes in cell proportions are reported as trends. In general, B cells and T cells were the most affected (Figure 4A-B). We observed a 33 % relative decrease in the proportion of B cells, a 39 % increase in CD4+ T cells, and an 195% (or 1.95 fold increase) increase in CD4+CD8+ T cells. A 22 % decrease in the proportion of acinar cells was also noted.

Differential expression analysis with SEURAT was performed between control and irradiated cell types. The complete list of differentially expressed genes (DEGs) is shown in supplementary file 3. CD4+CD8+ T-cells had the highest fold increase in cell number (~2 fold) after IR (Fig 4B) and the highest number of dysregulated genes (~70, but this is no on the graph) post-IR across all identified cell populations, followed by acinar cells (Figure 4C). We did not detect DEGs in MEC and stromal populations post-IR, and only 1 gene was differentially expressed in IR endothelial cells. The lack of DEGs in MECs is likely explained because of the low number of MECs analyzed (Figure 4B). Stromal and endothelial populations Stromal and endothelial cells also did not show significant changes in gene expression, but they were well-represented in our dataset; thus, cell numbers alone are not likely to account for the lack of DEGs post-IR in these populations. Instead, the lack of DEGs may reflect the fact that SG fibrosis does not consistently develop in mice post-IR. Alternatively, the endothelial and stromal populations may have recovered in this model a year after IR damage.

The top upregulated genes in acinar cells post-IR included *Actb, Tmsb4x*, and *Pfn1* which are involved in actin polymerization (Figure 4D). The genes *Gm42418, Hba-a1*, and *Smr3a* were the only downregulated genes in acinar cells and they were also downregulated in most other cell types (Figure S4A, Supplementary file 3), suggesting a global response to IR rather than an acinar-specific one. In CD4+CD8+ T-cells, the top upregulated genes post-IR were *Jun, Fos, Ltb*, *Klf2*, and *Klf6*, and the most downregulated genes were *Ctla2a, Tcp11l2, Crip1, Ramp3,* and *Tubb4b* (Figure 4D). In general, DEGs in acinar cells were associated with regulation of transepithelial transport, electron transport, apoptosis, and translation processes according to gene ontology

218 analysis via The Gene Ontology Consortium (The Gene Ontology Consortium, 2019), while
219 DEGs in CD4+CD8+ T-cells were associated with V(D)J recombination, lymphocyte
220 differentiation, apoptosis, axonogenesis, and ERK signaling pathway (Figure 4E).
221
222 **Predictive ligand-receptor analysis suggests dysregulation of cell-cell communication post-**
223 **IR in mouse PG**
224 To predict how gene expression alterations post-IR may impact cell-cell communication in
225 the gland, we performed ligand-receptor pair analysis focusing specifically on ligands and
226 receptors that were differentially expressed post-IR, particularly in acinar and CD4+CD8+ T-cells
227 which were the most transcriptionally affected. We identified 5 ligands (*Ptma, Hsp90aa1, Ltb,*
228 *Hspa1a,* and *Hras*) and 5 receptor genes (*Rpsa*, *Cd53, Ramp3, Cd28*, and *Ifngr1*) differentially
229 expressed post-IR in our dataset (Figure 5A-B). Although these genes were expressed across
230 multiple clusters and were not defining for any individual population, they were differentially
231 expressed in specific cell types. For instance, *Hsp90aa1* was downregulated in all immune
232 populations except NK cells and macrophages, and both *Hspa1a* and *Hras* were downregulated in
233 NK cells (Figure 5A). Similarly, *Rpsa* was upregulated in acinar cells while *Ifngr1* was
234 downregulated in CD4+CD8+ T-cells post-IR (Figure 5B). Putative pairs were found for *Rpsa*
235 (Ribosomal protein SA (*Rpsa*), also known as Laminin receptor 1), *Ifngr1* (Interferon Gamma
236 Receptor 1), *Hsp90aa1* (Heatshock protein 90 Alpha Family Class A Member 1), *Ltb*
237 (Lymphotoxin Beta), and *Hras* oncogene (Figure 5C).
238 When considering the directionality of expression changes in differentially expressed
239 ligands and receptors (upregulation vs downregulation) combined with the predicted interactions
240 with their corresponding pairs, our analysis suggested increased paracrine signaling to acinar cells
241 via *Lamb2-Rpsa* and decreased interactions between NK and CD8+ cells with CD4+CD8+ T-cells
242 via *Ifng-Ifngr1* (Figure 5C-D). Similarly, paracrine signaling via *Hsp90aa1* from immune cells to
243 *Egfr* expressed in myoepithelial, stromal, and endothelial cells was potentially reduced, while *Ltb*
244 interaction with *Tnfrsf1a* and *Cd40* expressed by macrophages, endothelial cells, dendritic cells,
245 and B-cells was potentially increased. Further studies are warranted to determine the functional
246 relevance of these predicted interactions.
247
248

Discussion

We previously generated a scRNAseq atlas of SMG development (Hauser *et al.*, 2020), and others have published limited scRNAseq studies primarily focused on describing the heterogeneity of SGs during homeostasis (Oyelakin *et al.*, 2019; Sekiguchi *et al.*, 2020). Here, we build on our previous work and generate a scRNAseq resource of adult PG that includes a chronic IR injury model. One of the major surprises of this resource is that CD4+CD8+ cells have the highest number of DEGs while acinar cells had the second largest number of DEGs post-IR. Changes in acinar cell transcription is not unexpected as IR often reduces saliva output. Our data suggest chronic post-IR damage may be sustained by immunologic mechanisms. Thus, providing mechanistic insights into the chronic damage to acinar cells post-IR. This is significant given the clinical need to develop therapies to regenerate acinar cells (Jensen et al., 2019). Furthermore, another surprising finding includes the characterization of a subpopulation of acinar and duct cells defined by expression of *Etv1* and *Erbb3* and the identification of putative ligand-receptor interactions between cell types during homeostasis and post-injury. For instance, Neuregulin 2 and 3 (Nrg2, Nrg3), which bind Erbb3 are primarily expressed in MECs, suggesting an interaction between MECs and Etv1+ cells. The significance of such interactions is covered in the next section.

Characterization of a subpopulation of Etv1+ epithelial cells

The development of single-cell RNA sequencing has allowed for high-throughput profiling of transcriptomes across cell types and states allowing for the detection of lowly expressed genes and rare cell types (Sandberg, 2014). Unbiased analysis of our data led to the identification of cell types present in the parotid SG including two distinct secretory populations (Acinar and *Etv1*+) based on their expression of Amylase 1 (*Amy1*). *Etv1* was recently associated with the development of the acinar epithelium in the mouse SMG but it is not known whether it represents a cell-type-specific marker or a cell state. The transcriptional profile of the *Etv1*+ population showed enrichment of *Erbb3* expression, which was supported by STITCH analysis. These findings are intriguing as Erbb3 signaling is critical for SG development and plays a crucial role in organogenesis. It has been shown previously that branching morphogenesis of the embryonic mouse SMG depends on intraepithelial signaling mediated by ErbB2, ErbB3, and neuregulin (NRG-1) (Miyazaki et al., 2004). Expression of ErbB3 was found mainly in the epithelium of the

developing murine SMG at E12-15 and epithelial morphogenesis occurring after E15 was reduced following treatment with an anti-NRG-1 neutralizing antibody. Additionally, Nrg1-null embryos show reduced innervation and defective branching morphogenesis (Mattingly et al., 2015; Nedvetsky et al., 2014). Thus, it is plausible that *Etv1*+ (*Erbb3+)* cells in the adult parotid gland could be involved in either replenishment of the epithelium or wound healing, and may function as a proacinar population in the PG. Furthermore, our data shows that Nrg1 and Nrg2 are differentially expressed by myoepithelial cells, suggesting paracrine regulation of this signaling via myoepithelial-*Etv1+:Erbb3*+ proacinar communication.

Applications of this resource to investigate intercellular communication

Cell-surface and transmembrane receptors confer cells with unique abilities to translate signals from their microenvironment into cellular outcomes, such as proliferation, migration, differentiation, response to infections, secretion, and contraction. Because receptors often bind multiple ligands, the exact outcome is determined by the specific ligand-receptor pair and the influence of coreceptors. A major advantage of scRNAseq is that it allows identification of ligand–receptor pairs to infer intercellular communication networks (Armingol et al., 2021) both in the context of tissue homeostasis and during injury. This information can be used to predict potential interactions that could be tested in models to ultimately improve cell-based therapies. For instance, the intercellular interactions that occur between acinar cells and their microenvironment are likely to influence their response to damage and their ability to regenerate.

Our finding that the neurotrophic receptor *Ntrk2* is enriched in acinar cells is interesting because of the precedent of using neurotrophic factors such as neurturin to preserve function in irradiated SGs (Ferreira *et al.*, 2018; Lombaert et al., 2020). Ligand-receptor analysis predicts that stromal and myoepithelial cells communicate with *Ntrk2*-expressing acinar cells via *Ntf5* and *Ntf3*, respectively. Considering the localization of myoepithelial cells surrounding acinar cells, it is likely that both juxtracrine and paracrine signaling takes place. The function of the Ntrk2 receptor in salivary acinar cells is not known but the gene is also highly expressed in Neurogenin 3-positive (Ngn3+) endocrine progenitors in the pancreas (Shamblott et al., 2016) and its activation regulates Ngn3+ cell fate commitment. Neurotrophin receptors are also mutated or upregulated in a variety of cancers, suggesting a role in proliferation and differentiation. In the SMG, *Ntrk2* is expressed in serous acinar cells but not in seromucous acinar cells (Hauser *et al.*, 2020), indicating that *Ntrk2*

signaling may be important for the serous acinar phenotype, which is predominant in the PG. Furthermore, we recently identified that *NTRK2* is highly upregulated in myoepithelial cells of irradiated human SGs along with other neurotrophin receptors and stimulation of neurotrophin signaling *in vitro* promoted myoepithelial differentiation (Chibly AM. *et al*. 2022). In the lacrimal gland, neurotrophins are expressed in acini while neurotrophin receptors are expressed by myoepithelial cells (Ghinelli et al., 2003), suggesting that neurotrophin signaling may mediate intercellular communication between acinar cells and myoepithelial cells in other exocrine tissues. Moreover, given that Ntrk2 is expressed on the cell surface, it may also provide a viable strategy to FACS-sort acinar cells from parotid gland to investigate expansion or differentiation of acinar cells *in vitro.* The latter application would likely require a combination of markers since *Ntrk2* is also expressed in *Etv1*+, myoepithelial and stromal cells.

Associations between epithelial and immune cells and the impact of radiation treatment.

There is growing evidence of immune-epithelial interactions in the regulation of tissue homeostasis and wound healing responses with macrophages and regulatory T-cells (T_{regs}; FoxP3+) garnering the most attention (Naik et al., 2018). Through Notch-mediated signaling, mammary gland stem cells induced resident macrophages to produce Wnt ligands ultimately leading to mammary stem cell proliferation (Chakrabarti et al., 2018). Depletion of T_{regs} in the intestine leads to a reduction in LGR5+ stem cells (Biton et al., 2018). Given the extensive ligand-receptor interactions between *Etv1*+ cells and immune cells, it is interesting to speculate a functional role of *Etv1*+ cells in directing the localization and activation of resident immune populations. In the epidermis, distinct cellular populations around the hair follicle produce distinct chemokines to direct innate immune cell populations (Mansfield and Naik, 2020). The interaction between *Etv1*+ and *FoxP3*+ cells via *Cdh1-Itae* (Table 1; encodes for E-cadherin and integrin-α-E) may represent the physical tethering of this sub-population of T-cells to the salivary epithelium under homeostasis (Agace et al., 2000). It's interesting to note that radiation treatment led to a 1.5-fold increase in T_{regs} without a concomitant change in *Etv1*+ cells or macrophages. Given the extensive role macrophages and *FoxP3*+ cells serve in injury and regeneration models, more work is required to unravel the impact of these T_{regs} -epithelial interactions population during SG dysfunction.

Radiation treatment also resulted in the greatest increase in CD4+CD8+ populations and the most DEGs observed in the CD4+CD8+ cells (Figure 4). Clinical evaluation of SMG by immunohistochemistry following radiotherapy has revealed increased T-cells (CD3+, CD4+ or CD8+) in the periacinar area and B cell (CD20+) nodules in the periductal area (Teymoortash et al., 2005). The DEGs in the CD4+CD8+ population suggest an imbalance in immune regulation following irradiation. Increases in KLF2 in IR PGs may represent a shift in T-cell populations as KLF2 is highly expressed in naïve and memory T-cells and downregulated by TCR activation and cytokine stimulation in effector T-cells (Preston et al., 2013). Additionally, high levels of KLF2 inhibit T-cell proliferation and clonal expansion (Preston *et al.*, 2013). KLF6 also inhibits cell proliferation and is co-regulated with KLF2 in MCF-7 cells (Ebert et al., 2012). Thus, high levels of KLF2 and KLF6 coupled with a lack of cytokines and chemokines on the DEGs suggest that the increase in CD4+CD8+ T-cells may represent a naïve population; however further kinetic analysis is required. This is also supported by a decrease in *Ctla2a,* which encodes for a cysteine protease that serves an immunosuppressive function in retinal pigment epithelium (Sugita et al., 2008; Sugita et al., 2009) and promotes the conversion of CD4+ T cells to Treg cells via Transforming Growth Factor Beta (TGFβ) signaling (Sugita et al., 2011). Lymphotoxin-β (LT-β), encoded by *Ltb*, is a TNF family member cytokine that has been predominantly studied in development and organization of lymphoid tissues (McCarthy et al., 2006). LT-β can mediate both regeneration and chronic tissue injury in epithelial organs via nuclear factor-κB (NF-κB) pathway (Tumanov et al., 2009; Wolf et al., 2010). Blocking the LT-β receptor suppresses immune responses by modulating trafficking mechanisms and disrupts the progression of T1DM in NOD mice (McCarthy *et al.*, 2006). It is interesting to speculate whether the increased LT-β interactions with *Tnfrsf1a* or *CD40* prevent the clearance of immune populations or maintenance of naïve T cells. *Ltb* is induced following oxidative stress (Wong, 1995) and has been proposed to enable communication between lymphocytes and stromal cells (Wolf *et al.*, 2010), findings that are corroborated by this work predicting increased interactions with stromal and immune cell populations post-IR (Figure 5).

Limitations of the study

A caveat of this study is the lack of isolation of basal ducts and peripheral nerve cells during PG dissociation, which were not represented. Similar limitations have been reported in other scRNAseq studies working with adult tissues, which could potentially be overcome using single nuclei RNAseq analysis. Furthermore, although multiple biological replicates were used, they were pooled together during dissociation prior to sequencing, thus, cell proportion changes should be considered with caution.

Lead contact

Further information and requests for resources and reagents should be directed to and will be fulfilled by the Lead Contact, Alejandro Chibly (martinez-chibly.agustin@gene.com)

Materials Availability

This study did not generate new unique reagents.

Data and Code Availability

The single-cell RNAseq libraries were deposited in GEO under accession number GSE####. The code used for analysis is available in github: https://github.com/chiblya/scRNAseq_PG. Ready-to-use Seurat objects are also available via figshare: 10.6084/m9.figshare.20406219

Methods

C3H mice and irradiation (IR) treatment

C3H female mice were used for the study and were housed at the NIDCR Veterinary Resource Core in accordance with IACUC guidelines. At 6-10 weeks of age, mice received IR treatment, which consisted a 6 Gy dose administered daily for 5 consecutive days. Mice were restrained using a Lucite Jig and IR treatment was targeted to the head and neck with an X-Rad 320ix system. The mice were housed for 10 months post-IR before scRNA-seq analysis.

Single-cell Dissociation. Parotid glands from 2 female mice per treatment were dissociated in a 15ml gentleMACS C tube with 5ml of digestion enzyme using the human tumor dissociation kit (#130-095-929, Miltenyi Biotech, Auburn CA) in RPMI 1640 w/L-Glutamine (Cell applications,

Inc, USA). Cell dissociation was performed in a Miltenyi gentleMACS Octo Dissociator using the manufacturer's preset 37C_h_TDK_2 program. Following dissociation, 5ml of RPMI media were added to the dissociated cells and centrifuged at 1100 rpm for 10 min. Cells were resuspended in RPMI 1640 w/L-Glutamine with 5% PenStrep (Gibco, USA) and washed twice with RPMI. Cells were passed through 70 µm filters between centrifugation steps. Single-cell dissociation was confirmed by microscopic examination and cell concentration determined with a Cellometer (Nexcelom Biosciences). Cell concentration was adjusted to $5x10^5$ – $1x10^6$ cells/ml prior to analysis with a 10X genomics Next GEM Chromium controller.

Library prep and sequencing: Single-cell RNA-seq library preparation was performed at the NIDCR Genomics and Computational Biology Core using a Chromium Single Cell v3 method (10X Genomics) following the manufacturer's protocol. Pooled single-cell RNA-seq libraries were sequenced on a NextSeq500 sequencer (Illumina). Cell Ranger Single-Cell Software Suite (10X Genomics) was used for demultiplexing, barcode assignment, and unique molecular identifier (UMI) quantification using the mm10 reference genome (Genome Reference Consortium Mouse Build 38) for read alignment.

Computational analysis: Cell Ranger files were imported to SEURAT v3 using R & R Studio software and processed for clustering following their default pipeline. As a quality control measure, cells with fewer than 200 genes were not included in subsequent analyses, and those with >5% of UMIs mapping to mitochondrial genes were defined as non-viable or apoptotic and were also excluded. Normalization and scaling were performed following SEURAT's default pipeline. Data from control and irradiated glands were bioinformatically integrated prior to assigning cell annotations. 'Clustree' package was used to determine an optimal resolution for clustering and the resulting clusters were annotated based on the expression of known cell type markers. Cell-defining genes were determined using the 'FindAllMarkers' function which uses a Wilcoxon Rank Sum statistical test for analysis. Only genes with adjusted p-values <0.05 were considered as cell-defining genes. To identify differentially expressed genes between treatments, each population was compared individually using the 'FindMarkers' function from SEURAT package.

434 **Ligand-receptor analysis**

435 A database of curated ligand-receptor pairs was downloaded from Ramikowski *et al.* (2015). We
436 used scripted code in R to automate the search for ligand and receptor genes within our dataset and
437 leverage that information against the curated database. Plots were generated using the 'circlize'
438 package in R. The code is available as supplementary material.

439

440 **Immunohistochemistry**: PGs were fixed in 4% paraformaldehyde overnight at 4°C and
441 dehydrated with 70% Ethanol prior to paraffin embedding. 5µm sections were deparaffinized with
442 xylene substitute for 10 minutes and rehydrated with reverse ethanol gradient for 5 minutes each.
443 Heat induced antigen retrieval was performed using a microwave maintaining sub-boiling
444 temperature for 10 minutes in a pH 6.0 Citrate Buffer (#21545, EDM Millipore, Darmstadt,
445 Germany) . Sections were washed for 5 minutes with 0.1% Tween20 (Quality Biological, Inc) in
446 PBS 1X (PBST). M.O.M.® (Mouse on Mouse) Immunodetection Kit (Vector Laboratories,
447 Burlingame, CA) was used to block non-specific sites for 1 hour at room temperature followed by
448 overnight incubation with primary antibodies at 4°C. Tissue sections were washed 3 times for 5
449 minutes each with PBST and incubated in secondary antibodies and nuclear stain (Hoechst
450 (Thermo Fisher Scientific, Marietta, OH)) at room temperature for 1 hour. Coverslips were
451 mounted with Fluoro-Gel (Electron Microscopy Sciences, Hatfield, PA), and imaging was
452 performed with a Nikon A1R confocal system.

453

454 **Stitch analysis:** Etv1+ cell defining genes from control parotid sample (Supplementary File 1)
455 were directly imported into STITCH (http://stitch.embl.de/). For reproducibility, analysis was
456 performed selecting a minimum interaction score of 0.7 and limited to less than 10 interactions.

457

458 **Acknowledgments**

459 The authors thank the support from Dr. Daniel Martin, Dr. Robert Morell, and Dr. Erich Boger
460 from the Genomics and computational biology core (GCBC) at NIDCR for contributing to library
461 preparation and sequencing. This work used the NIDCR Veterinary Resources Core (ZIC
462 DE000740-05) and computational resources of the NIH HPC Biowulf cluster (http://hpc.nih.gov).
463 The GCBC funds were from the NIDCD Division of Intramural Research/NIH (DC000086 to the

GCBC). The study was supported by the Intramural Research Program of the National Institute of Dental and Craniofacial Research, NIH.

Author Contributions

Conceptualization, writing and editing, A.M.C, B.R, K.H.L; Methodology, A.M.C., B.R., M.C.P., GCBC; Software, A.M.C, GCBC; Resources, M.P.H, K.H.L., A.M.C; Visualization, A.M.C., B.R., M.C.P; Data curation, project administration, and supervision, A.M.C.

Declaration of Interests

The authors declare no competing interests.

Figure Legends

Figure 1. scRNAseq analysis of control and irradiated PG

A) Single cell suspensions from 1-year-old control and irradiated PG from 2 C3H female mice were used to build scRNAseq libraries. Representative UMAP plots are colored by treatment group or cell type. Clusters were annotated based on the expression of known markers.

B) Balloon Plot with top 5 differentially expressed genes per cluster sorted by fold change. Statistical analysis performed using SEURAT package in R. Color is relative to scaled gene expression and size of the dot represents the percentage of cells expressing the gene.

C) Representative UMAP plots showing expression of Etv1 and Amy1

Figure 2. scRNAseq analysis of control and irradiated PG

A) UMAP plot highlighting acinar, Etv1+, and duct populations with a representative heatmap of their gene expression profiles.

B) Venn diagram of cell-defining genes in acinar and Etv1+ clusters showing the number of unique and overlapping cell-defining genes. Representative genes from each group are shown. The bar graph shows the percentage of overlap between cell-defining genes in acinar and duct populations with Etv1+ cells.

C) Balloon plot showing expression of the 30 genes overlapping between acinar and Etv1+ cells. Genes marked with an asterisk are differentially expressed between Etv1+ and acinar cells ($p<0.05$, Wilcoxon rank sum test (SEURAT)). Color is relative to scaled gene expression and size of the dot represents the percentage of cells within a cluster expressing the gene.

D) Immunofluorescence staining of PG from 1 year-old C3H mice stained for Etv1 (Red), NKCC1 (green) and DAPI (blue). The area delineated by the yellow dotted line is magnified to the right for visualization. Scale bar = 50um.

E) Results from STITCH analysis showing top biological processes and KEGG pathways associated with defining-genes from Etv1+ cells.

Figure 3. Ligand-receptor analysis of Etv1+ and acinar cells

A) Bar graphs with number of identified ligands and receptors among cell-defining genes from epithelial populations.

B) Balloon plots of expression of ligands and receptors enriched in Etv1+ cells.

C) Balloon plots of expression of ligands and receptors enriched in acinar cells.

D) Chord plot summarizing putative ligand-receptor interactions with Etv1+ cell ligands. The arrows point to the cell expressing the corresponding receptors and are color-coded based on the source of the ligand. The thickness of the arrow is relative to the number of putative pairs identified between Etv1 cells and the cell type pointed by the arrow. Representative ligand-receptor pairs are shown beside the chord plots.

E) Chord plot summarizing putative ligand-receptor interactions with Etv1+ cell receptors.

F) Immunofluorescence staining for Smooth muscle actin (SMA, Red), NTRK2 (green) and Parotid Secretory Protein (PSP, blue). The area delineated by the yellow dotted line is magnified to the right for visualization. Scale bar = 50um.

Figure 4. Cell-specific IR-induced DEGs

A) Representative UMAP of irradiated PG colored by cell type.

B) Cell numbers and proportions in scRNAseq datasets from control and irradiated PG.

C) Bar graph showing number of differentially expressed genes (DEGs) post-IR in individual cell populations. DE analysis was performed with SEURAT's default Wilcoxon test ($p<0.05$).

D) Violin plots of top 5 (if present) up and downregulated genes in acinar and CD4+CD8+ T-cells. Red and blue arrows denote upregulated and downregulated genes, respectively.

E) Representative output from gene ontology analysis with IR-induced DEGs in acinar and CD4+CD8+ T-cells showing dysregulated processes and their associated genes.

Figure 5. Dysregulated ligand-receptor pairs post-IR

A) Violin plots of differentially expressed receptors.

B) Violin plots of differentially expressed ligands.

C) Chord plot of ligand-receptor interactions with IR-induced DE receptors

D) Chord plot of ligand-receptor interactions with IR-induced DE ligands

E) Summary table with putative ligand-receptor interactions with IR-induced ligands and receptors

References

Agace, W.W., Higgins, J.M., Sadasivan, B., Brenner, M.B., and Parker, C.M. (2000). T-lymphocyte-epithelial-cell interactions: integrin alpha(E)(CD103)beta(7), LEEP-CAM and chemokines. Curr Opin Cell Biol *12*, 563-568. 10.1016/s0955-0674(00)00132-0.

Armingol, E., Officer, A., Harismendy, O., and Lewis, N.E. (2021). Deciphering cell–cell interactions and communication from gene expression. Nature Reviews Genetics *22*, 71-88. 10.1038/s41576-020-00292-x.

Biton, M., Haber, A.L., Rogel, N., Burgin, G., Beyaz, S., Schnell, A., Ashenberg, O., Su, C.-W., Smillie, C., Shekhar, K., et al. (2018). T Helper Cell Cytokines Modulate Intestinal Stem Cell Renewal and Differentiation. Cell *175*, 1307-1320.e1322. https://doi.org/10.1016/j.cell.2018.10.008.

Chakrabarti, R., Celià-Terrassa, T., Kumar, S., Hang, X., Wei, Y., Choudhury, A., Hwang, J., Peng, J., Nixon, B., Grady, J.J., et al. (2018). Notch ligand Dll1 mediates cross-talk between mammary stem cells and the macrophageal niche. Science *360*, eaan4153. 10.1126/science.aan4153.

Chen, M., Lin, W., Gan, J., Lu, W., Wang, M., Wang, X., Yi, J., and Zhao, Z. (2022). Transcriptomic Mapping of Human Parotid Gland at Single-Cell Resolution. J Dent Res *101*, 972-982. 10.1177/00220345221076069.

Dirix, P., Nuyts, S., and Van den Bogaert, W. (2006). Radiation-induced xerostomia in patients with head and neck cancer: a literature review. Cancer *107*, 2525-2534. 10.1002/cncr.22302.

Ebert, R., Zeck, S., Meissner-Weigl, J., Klotz, B., Rachner, T.D., Benad, P., Klein-Hitpass, L., Rudert, M., Hofbauer, L.C., and Jakob, F. (2012). Krüppel-like factors KLF2 and 6 and Ki-67 are direct targets of zoledronic acid in MCF-7 cells. Bone *50*, 723-732. https://doi.org/10.1016/j.bone.2011.11.025.

Eisbruch, A., Ten Haken, R.K., Kim, H.M., Marsh, L.H., and Ship, J.A. (1999). Dose, volume, and function relationships in parotid salivary glands following conformal and intensity-modulated irradiation of head and neck cancer. Int J Radiat Oncol Biol Phys *45*, 577-587. 10.1016/s0360-3016(99)00247-3.

Ferreira, J.N.A., Zheng, C., Lombaert, I.M.A., Goldsmith, C.M., Cotrim, A.P., Symonds, J.M., Patel, V.N., and Hoffman, M.P. (2018). Neurturin Gene Therapy Protects Parasympathetic Function to Prevent Irradiation-Induced Murine Salivary Gland Hypofunction. Molecular Therapy - Methods & Clinical Development *9*, 172-180. https://doi.org/10.1016/j.omtm.2018.02.008.

Gao, X., Oei, M.S., Ovitt, C.E., Sincan, M., and Melvin, J.E. (2018). Transcriptional profiling reveals gland-specific differential expression in the three major salivary glands of the adult mouse. Physiological Genomics *50*, 263-271. 10.1152/physiolgenomics.00124.2017.

Ghinelli, E., Johansson, J., Ríos, J.D., Chen, L.-L., Zoukhri, D., Hodges, R.R., and Dartt, D.A. (2003). Presence and Localization of Neurotrophins and Neurotrophin Receptors in Rat Lacrimal Gland. Investigative Ophthalmology & Visual Science *44*, 3352-3357. 10.1167/iovs.03-0037.

Grün, D., and van Oudenaarden, A. (2015). Design and Analysis of Single-Cell Sequencing Experiments. Cell *163*, 799-810. https://doi.org/10.1016/j.cell.2015.10.039.

Grundmann, O., Mitchell, G.C., and Limesand, K.H. (2009). Sensitivity of Salivary Glands to Radiation: from Animal Models to Therapies. Journal of Dental Research *88*, 894-903. 10.1177/0022034509343143.

Hauser, B.R., Aure, M.H., Kelly, M.C., Hoffman, M.P., and Chibly, A.M. (2020). Generation of a Single-Cell RNAseq Atlas of Murine Salivary Gland Development. iScience *23*, 101838. https://doi.org/10.1016/j.isci.2020.101838.

Henson, B.S., Eisbruch, A., D'Hondt, E., and Ship, J.A. (1999). Two-year longitudinal study of parotid salivary flow rates in head and neck cancer patients receiving unilateral neck parotid-sparing radiotherapy treatment. Oral Oncology *35*, 234-241. https://doi.org/10.1016/S1368-8375(98)00104-3.

Huang, N., Perez, P., Kato, T., Mikami, Y., Okuda, K., Gilmore, R.C., Conde, C.D., Gasmi, B., Stein, S., Beach, M., et al. (2021). SARS-CoV-2 infection of the oral cavity and saliva. Nat Med *27*, 892-903. 10.1038/s41591-021-01296-8.

Jensen, S.B., Pedersen, A.M., Vissink, A., Andersen, E., Brown, C.G., Davies, A.N., Dutilh, J., Fulton, J.S., Jankovic, L., Lopes, N.N., et al. (2010). A systematic review of salivary gland hypofunction and xerostomia induced by cancer therapies: prevalence, severity and impact on quality of life. Support Care Cancer *18*, 1039-1060. 10.1007/s00520-010-0827-8.

Jensen, S.B., Vissink, A., Limesand, K.H., and Reyland, M.E. (2019). Salivary Gland Hypofunction and Xerostomia in Head and Neck Radiation Patients. J Natl Cancer Inst Monogr *2019*. 10.1093/jncimonographs/lgz016.

Kolodziejczyk, Aleksandra A., Kim, J.K., Svensson, V., Marioni, John C., and Teichmann, Sarah A. (2015). The Technology and Biology of Single-Cell RNA Sequencing. Molecular Cell *58*, 610-620. https://doi.org/10.1016/j.molcel.2015.04.005.

Kuhn, M., von Mering, C., Campillos, M., Jensen, L.J., and Bork, P. (2008). STITCH: interaction networks of chemicals and proteins. Nucleic Acids Res *36*, D684-688. 10.1093/nar/gkm795.

Li, Y., Taylor, J.M., Ten Haken, R.K., and Eisbruch, A. (2007). The impact of dose on parotid salivary recovery in head and neck cancer patients treated with radiation therapy. Int J Radiat Oncol Biol Phys *67*, 660-669. 10.1016/j.ijrobp.2006.09.021.

Lombaert, I.M.A., Patel, V.N., Jones, C.E., Villier, D.C., Canada, A.E., Moore, M.R., Berenstein, E., Zheng, C., Goldsmith, C.M., Chorini, J.A., et al. (2020). CERE-120 Prevents Irradiation-Induced Hypofunction and Restores Immune Homeostasis in Porcine Salivary Glands. Molecular Therapy - Methods & Clinical Development *18*, 839-855. https://doi.org/10.1016/j.omtm.2020.07.016.

Mansfield, K., and Naik, S. (2020). Unraveling Immune-Epithelial Interactions in Skin Homeostasis and Injury. Yale J Biol Med *93*, 133-143.

Mattingly, A., Finley, J.K., and Knox, S.M. (2015). Salivary gland development and disease. Wiley Interdiscip Rev Dev Biol *4*, 573-590. 10.1002/wdev.194.

McCarthy, D.D., Summers-Deluca, L., Vu, F., Chiu, S., Gao, Y., and Gommerman, J.L. (2006). The lymphotoxin pathway. Immunologic Research *35*, 41-53. 10.1385/IR:35:1:41.

Miyazaki, Y., Nakanishi, Y., and Hieda, Y. (2004). Tissue interaction mediated by neuregulin-1 and ErbB receptors regulates epithelial morphogenesis of mouse embryonic submandibular gland. Dev Dyn *230*, 591-596. 10.1002/dvdy.20078.

Mukherjee, A., Epperly, M.W., Shields, D., Hou, W., Fisher, R., Hamade, D., Wang, H., Saiful Huq, M., Bao, R., Tabib, T., et al. (2021). Ionizing irradiation-induced Fgr in senescent cells mediates fibrosis. Cell Death Discov *7*, 349. 10.1038/s41420-021-00741-4.

Naik, S., Larsen, S.B., Cowley, C.J., and Fuchs, E. (2018). Two to Tango: Dialog between Immunity and Stem Cells in Health and Disease. Cell *175*, 908-920. https://doi.org/10.1016/j.cell.2018.08.071.

Nedvetsky, Pavel I., Emmerson, E., Finley, Jennifer K., Ettinger, A., Cruz-Pacheco, N., Prochazka, J., Haddox, Candace L., Northrup, E., Hodges, C., Mostov, Keith E., et al. (2014). Parasympathetic Innervation Regulates Tubulogenesis in the Developing Salivary Gland. Developmental Cell *30*, 449-462. https://doi.org/10.1016/j.devcel.2014.06.012.

Oyelakin, A., Song, E.A.C., Min, S., Bard, J.E., Kann, J.V., Horeth, E., Smalley, K., Kramer, J.M., Sinha, S., and Romano, R.A. (2019). Transcriptomic and Single-Cell Analysis of the Murine Parotid Gland. J Dent Res *98*, 1539-1547. 10.1177/0022034519882355.

Paldor, M., Levkovitch-Siany, O., Eidelshtein, D., Adar, R., Enk, C.D., Marmary, Y., Elgavish, S., Nevo, Y., Benyamini, H., Plaschkes, I., et al. (2022). Single-cell transcriptomics reveals a

senescence-associated IL-6/CCR6 axis driving radiodermatitis. EMBO Mol Med, e15653. 10.15252/emmm.202115653.

Preston, G.C., Feijoo-Carnero, C., Schurch, N., Cowling, V.H., and Cantrell, D.A. (2013). The Impact of KLF2 Modulation on the Transcriptional Program and Function of CD8 T Cells. PLOS ONE *8*, e77537. 10.1371/journal.pone.0077537.

Radfar, L., and Sirois, D.A. (2003). Structural and functional injury in minipig salivary glands following fractionated exposure to 70 Gy of ionizing radiation: an animal model for human radiation-induced salivary gland injury. Oral Surg Oral Med Oral Pathol Oral Radiol Endod *96*, 267-274. 10.1016/s1079-2104(03)00369-x.

Ramilowski, J.A., Goldberg, T., Harshbarger, J., Kloppmann, E., Lizio, M., Satagopam, V.P., Itoh, M., Kawaji, H., Carninci, P., Rost, B., and Forrest, A.R. (2015). A draft network of ligand-receptor-mediated multicellular signalling in human. Nat Commun *6*, 7866. 10.1038/ncomms8866.

Robar, J.L., Day, A., Clancey, J., Kelly, R., Yewondwossen, M., Hollenhorst, H., Rajaraman, M., and Wilke, D. (2007). Spatial and dosimetric variability of organs at risk in head-and-neck intensity-modulated radiotherapy. Int J Radiat Oncol Biol Phys *68*, 1121-1130. 10.1016/j.ijrobp.2007.01.030.

Sandberg, R. (2014). Entering the era of single-cell transcriptomics in biology and medicine. Nat Methods *11*, 22-24. 10.1038/nmeth.2764.

Sekiguchi, R., Martin, D., Genomics, Computational Biology, C., and Yamada, K.M. (2020). Single-Cell RNA-seq Identifies Cell Diversity in Embryonic Salivary Glands. J Dent Res *99*, 69-78. 10.1177/0022034519883888.

Shamblott, M.J., O'Driscoll, M.L., Gomez, D.L., and McGuire, D.L. (2016). Neurogenin 3 is regulated by neurotrophic tyrosine kinase receptor type 2 (TRKB) signaling in the adult human exocrine pancreas. Cell Communication and Signaling *14*, 23. 10.1186/s12964-016-0146-x.

Stuart, T., Butler, A., Hoffman, P., Hafemeister, C., Papalexi, E., Mauck, W.M., Hao, Y., Stoeckius, M., Smibert, P., and Satija, R. (2019). Comprehensive Integration of Single-Cell Data. Cell *177*, 1888-1902.e1821. https://doi.org/10.1016/j.cell.2019.05.031.

Sugita, S., Horie, S., Nakamura, O., Futagami, Y., Takase, H., Keino, H., Aburatani, H., Katunuma, N., Ishidoh, K., Yamamoto, Y., and Mochizuki, M. (2008). Retinal Pigment Epithelium-Derived CTLA-2α Induces TGFβ-Producing T Regulatory Cells. The Journal of Immunology *181*, 7525. 10.4049/jimmunol.181.11.7525.

Sugita, S., Horie, S., Nakamura, O., Maruyama, K., Takase, H., Usui, Y., Takeuchi, M., Ishidoh, K., Koike, M., Uchiyama, Y., et al. (2009). Acquisition of T Regulatory Function in Cathepsin L-Inhibited T Cells by Eye-Derived CTLA-2α during Inflammatory Conditions. The Journal of Immunology *183*, 5013. 10.4049/jimmunol.0901623.

Sugita, S., Yamada, Y., Horie, S., Nakamura, O., Ishidoh, K., Yamamoto, Y., Yamagami, S., and Mochizuki, M. (2011). Induction of T Regulatory Cells by Cytotoxic T-Lymphocyte Antigen-2α on Corneal Endothelial Cells. Investigative Ophthalmology & Visual Science *52*, 2598-2605. 10.1167/iovs.10-6322.

Tabula Muris, C., Overall, c., Logistical, c., Organ, c., processing, Library, p., sequencing, Computational data, a., Cell type, a., Writing, g., et al. (2018). Single-cell transcriptomics of 20 mouse organs creates a Tabula Muris. Nature *562*, 367-372. 10.1038/s41586-018-0590-4.

Tabula Sapiens, C., Jones, R.C., Karkanias, J., Krasnow, M.A., Pisco, A.O., Quake, S.R., Salzman, J., Yosef, N., Bulthaup, B., Brown, P., et al. (2022). The Tabula Sapiens: A multiple-organ, single-cell transcriptomic atlas of humans. Science *376*, eabl4896. 10.1126/science.abl4896.

Teos, L.Y., Zheng, C.Y., Liu, X., Swaim, W.D., Goldsmith, C.M., Cotrim, A.P., Baum, B.J., and Ambudkar, I.S. (2016). Adenovirus-mediated hAQP1 expression in irradiated mouse salivary glands causes recovery of saliva secretion by enhancing acinar cell volume decrease. Gene Therapy *23*, 572-579. 10.1038/gt.2016.29.

Teymoortash, A., Simolka, N., Schrader, C., Tiemann, M., and Werner, J.A. (2005). Lymphocyte subsets in irradiation-induced sialadenitis of the submandibular gland. Histopathology *47*, 493-500. 10.1111/j.1365-2559.2005.02256.x.

The Gene Ontology Consortium (2019). The Gene Ontology Resource: 20 years and still GOing strong. Nucleic Acids Research *47*, D330-D338. 10.1093/nar/gky1055.

Trapnell, C. (2015). Defining cell types and states with single-cell genomics. Genome Res *25*, 1491-1498. 10.1101/gr.190595.115.

Tumanov, A.V., Koroleva, E.P., Christiansen, P.A., Khan, M.A., Ruddy, M.J., Burnette, B., Papa, S., Franzoso, G., Nedospasov, S.A., Fu, Y.X., and Anders, R.A. (2009). T Cell-Derived Lymphotoxin Regulates Liver Regeneration. Gastroenterology *136*, 694-704.e694. https://doi.org/10.1053/j.gastro.2008.09.015.

Vissink, A., Mitchell, J.B., Baum, B.J., Limesand, K.H., Jensen, S.B., Fox, P.C., Elting, L.S., Langendijk, J.A., Coppes, R.P., and Reyland, M.E. (2010). Clinical management of salivary gland hypofunction and xerostomia in head-and-neck cancer patients: successes and barriers. Int J Radiat Oncol Biol Phys *78*, 983-991. 10.1016/j.ijrobp.2010.06.052.

Wang, Y., and Navin, Nicholas E. (2015). Advances and Applications of Single-Cell Sequencing Technologies. Molecular Cell *58*, 598-609. https://doi.org/10.1016/j.molcel.2015.05.005.

Wolf, M.J., Seleznik, G.M., Zeller, N., and Heikenwalder, M. (2010). The unexpected role of lymphotoxin β receptor signaling in carcinogenesis: from lymphoid tissue formation to liver and prostate cancer development. Oncogene *29*, 5006-5018. 10.1038/onc.2010.260.

Wong, G.H.W. (1995). Protective roles of cytokines against radiation: Induction of mitochondrial MnSOD. Biochimica et Biophysica Acta (BBA) - Molecular Basis of Disease *1271*, 205-209. https://doi.org/10.1016/0925-4439(95)00029-4.

Xu, Y., Feng, S., Peng, Q., Zhu, W., Zu, Q., Yao, X., Zhang, Q., Cao, J., and Jiao, Y. (2021). Single-cell RNA sequencing reveals the cell landscape of a radiation-induced liver injury mouse model. Radiation Medicine and Protection *2*, 181-183. 10.1016/j.radmp.2021.11.001.

Zappia, L., and Oshlack, A. (2018). Clustering trees: a visualization for evaluating clusterings at multiple resolutions. GigaScience *7*. 10.1093/gigascience/giy083.

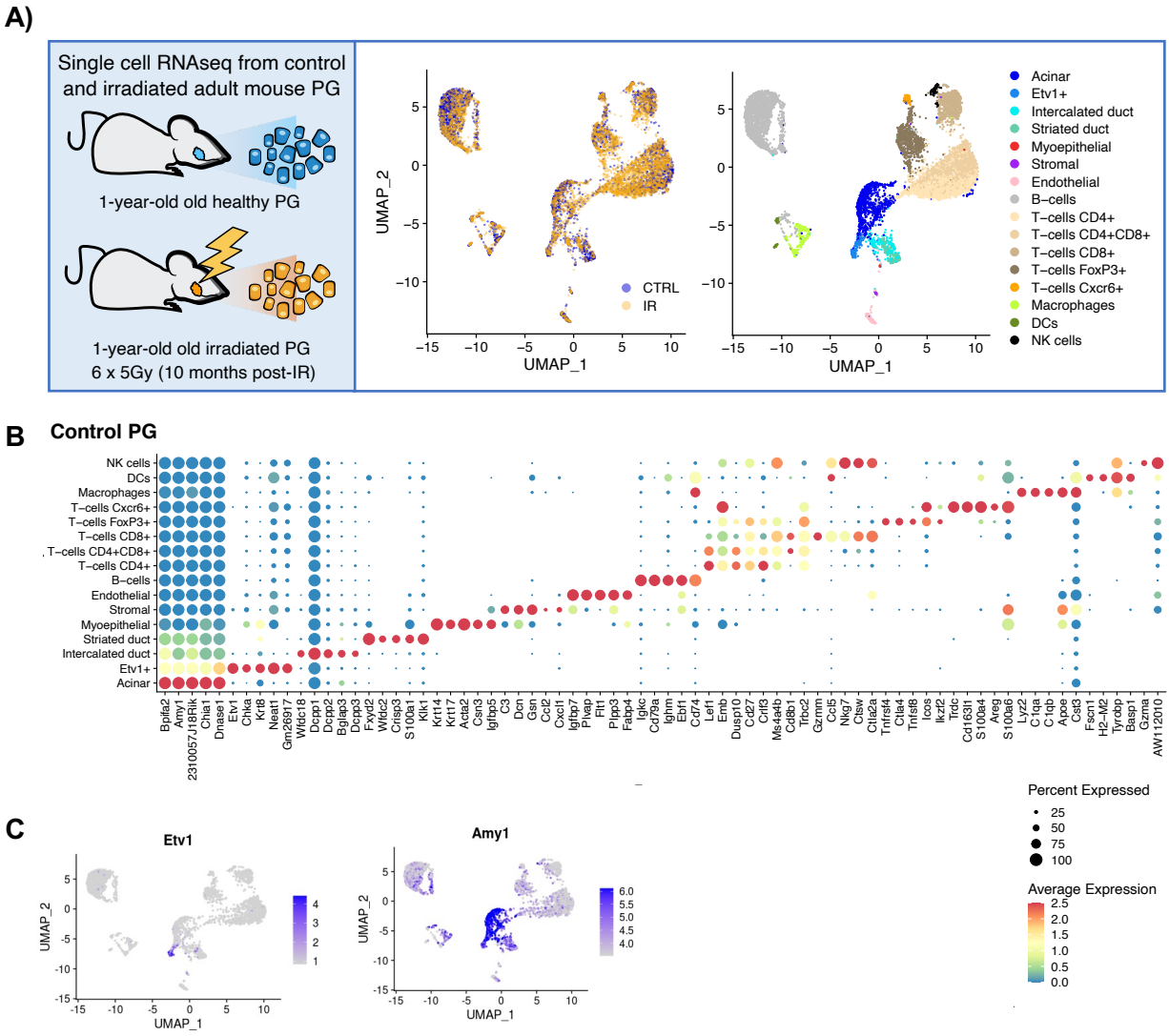

Figure 1. scRNAseq analysis of control and irradiated PG

A) Single cell suspensions from 1-year-old control and irradiated PG from 2 C3H female mice were used to build scRNAseq libraries. Representative UMAP plots are colored by treatment group or cell type. Clusters were annotated based on the expression of known markers.

B) Balloon Plot showing expression of the top 5 differentially expressed genes per cluster sorted by fold change. Statistical analysis performed using SEURAT package in R. Color is relative to scaled gene expression and size of the dot represents the percentage of cells expressing the gene.

C) Representative UMAP plots showing expression of Etv1 and Amy1

Figure S1, related to Figure 1

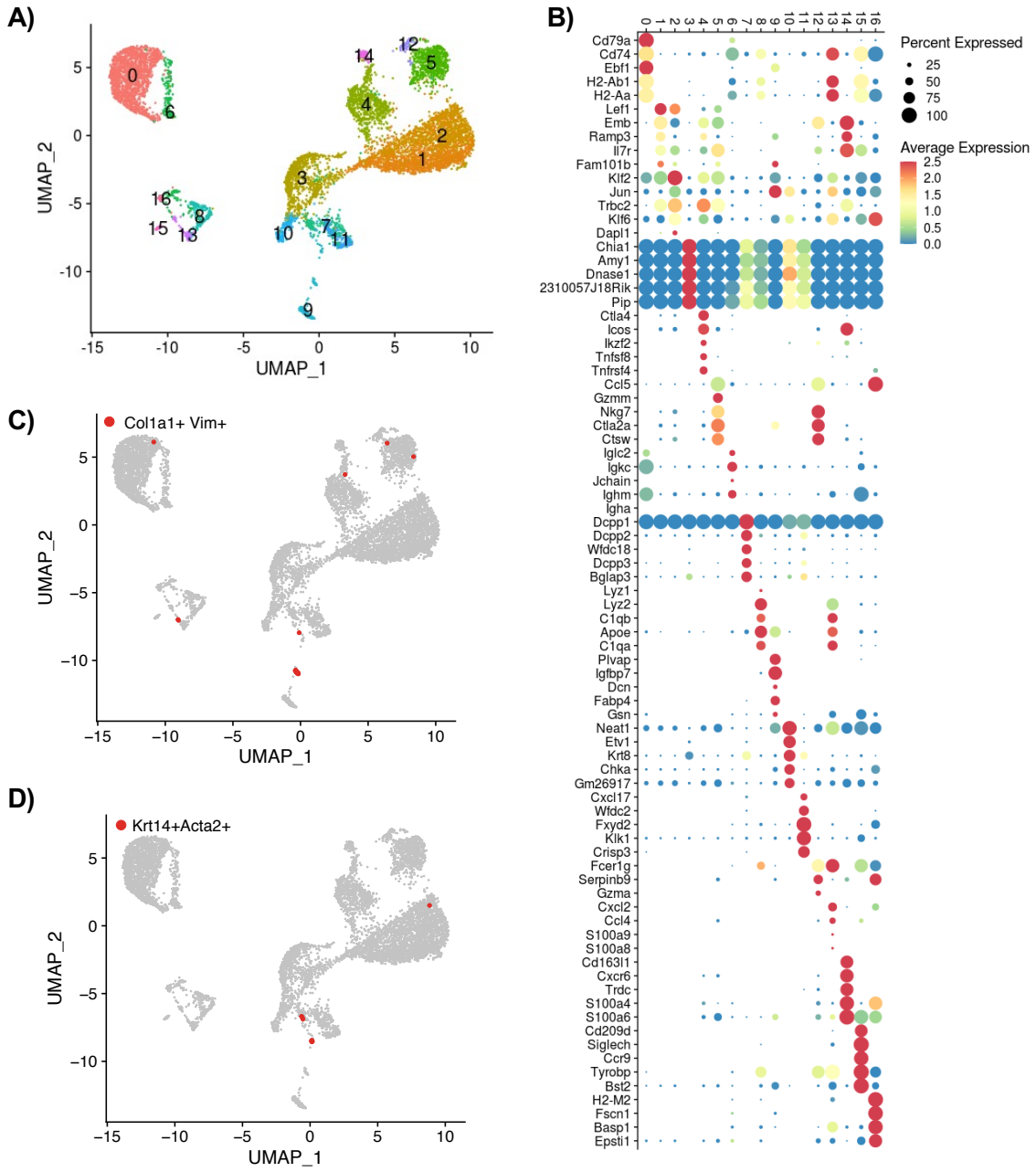

Figure S1: Annotation strategy

A) Unsupervised clustering of integrated control and irradiated mouse parotid gland (n=1 per treatment)

B) Balloon plot of top cluster-defining genes. Color is relative to scaled gene expression and size of the dot represents the percentage of cells within a cluster expressing the gene

C) UMAP highlighting cells that express the stromal markers Col1a1 and Vim

D) UMAP highlighting myoepithelial cells that express Krt14 and Acta2

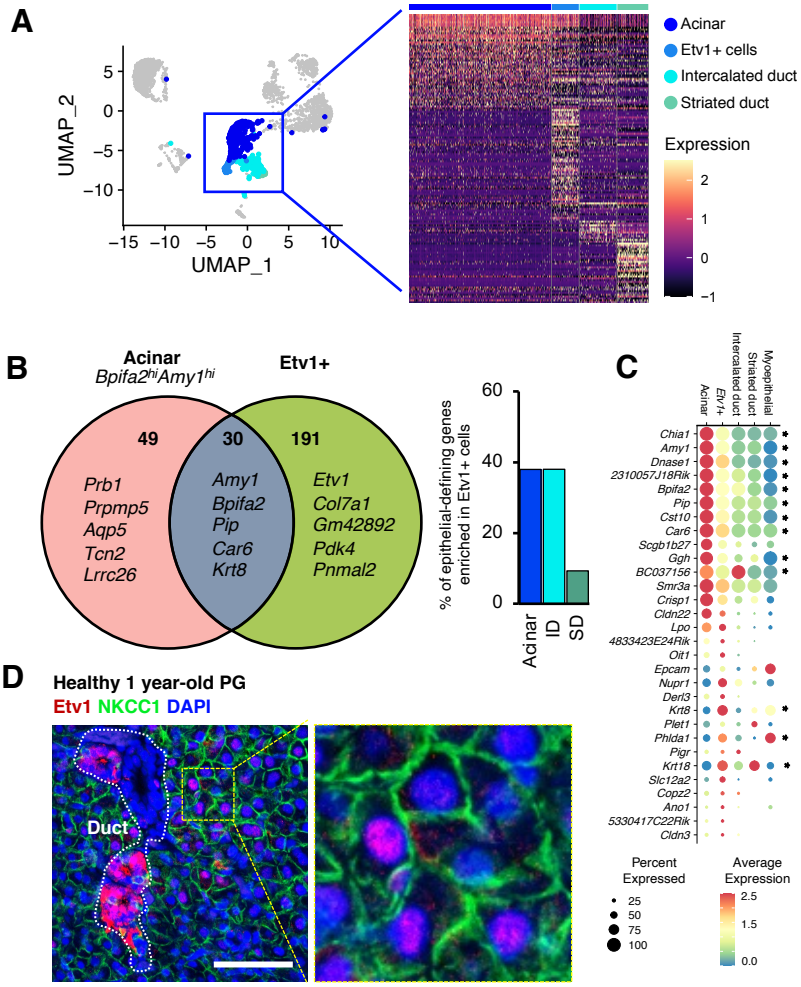

E

GO Biological Processes			
Pathway ID	**Pathway description**	**Gene count**	**FDR**
GO.0048519	Negative regulation of biological process	68	6.27E-08
GO.0009888	Tissue development	40	8.90E-08
GO.0048513	Organ development	53	1.59E-07
GO.0048523	Negative regulation of cellular process	63	1.59E-07
GO.0031325	Positive regulation of metabolic process	51	3.08E-07
KEGG pathways			
Pathway ID	**Pathway description**	**Gene count**	**FDR**
4015	Rap1 signaling pathway	13	4.92E-06
5210	Colorectal cancer	8	6.08E-06
4668	TNF signaling pathway	8	0.000203
5161	Hepatitis B	9	0.000203
4012	ErbB signaling pathway	7	0.000291

Figure 2. scRNAseq analysis of control and irradiated PG

A) UMAP plot highlighting acinar, Etv1+, and duct populations with a representative heatmap of their gene expression profiles.
B) Venn diagram of cell-defining genes in acinar and Etv1+ clusters showing the number of unique and overlapping cell-defining genes. Representative genes from each group are shown. The bar graph shows the percentage of overlap between cell-defining genes in acinar and duct populations with Etv1+ cells.
C) Balloon plot showing expression of 30 cell-defining genes overlapping between acinar and Etv1+ cells. Genes marked with an asterisk are differentially expressed between Etv1+ and Acinar cells ($p<0.05$, Wilcoxon rank sum test (SEURAT)). Color is relative to scaled gene expression and size of the dot represents the percentage of cells within a cluster expressing the gene.
D) Immunofluorescence staining of PG from 1 year-old C3H mice stained for Etv1 (Red), NKCC1 (green) and DAPI (blue). The area delineated by the yellow dotted line is magnified to the right for visualization. Scale bar = 50um.
E) Results from STITCH analysis showing top biological processes and KEGG pathways associated with defining-genes from Etv1+ cells.

Figure S2, related to Figure 2

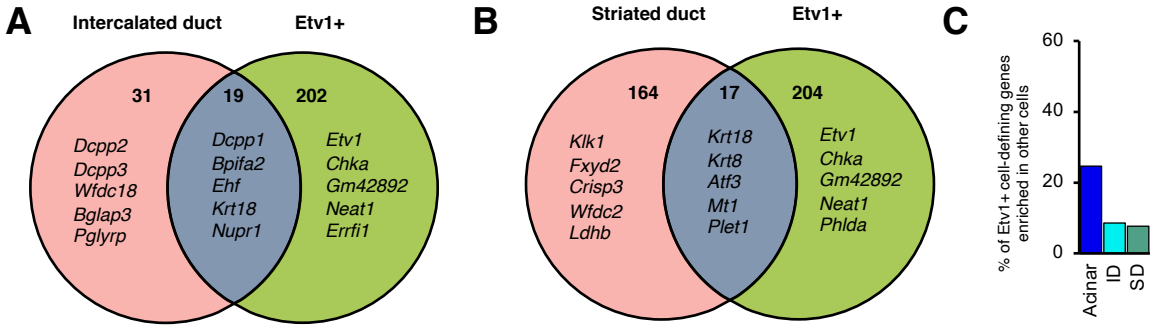

D

GO Biological Processes (Acinar cells)			
Pathway ID	**Pathway description**	**Gene count**	**FDR**
GO.0002018	renin-angiotensin regulation of aldosterone production	3	0.000359
GO.0003081	regulation of systemic arterial blood pressure by renin-angiotensin	5	0.000359
GO.0003073	regulation of systemic arterial blood pressure	6	0.00163
GO.0002035	brain renin-angiotensin system	3	0.00227
GO.0050708	regulation of protein secretion	9	0.00476
KEGG pathways (Acinar cells)			
Pathway ID	**Pathway description**	**Gene count**	**FDR**
4614	Renin-angiotensin system	5	2.21E-06
4150	mTOR signaling pathway	5	0.000499
4970	Salivary secretion	5	0.000867

Figure S2.

A) Venn diagram comparing defining genes for *Etv1*+ and ID populations. The numbers in the left and right panels indicates the number of unique genes in the corresponding population whereas the number in the central panel reflects the overlap between the two populations.

B) Venn diagram comparing defining genes for *Etv1*+ and SD populations. The numbers in the left and right panels indicates the number of unique genes in the corresponding population whereas the number in the central panel reflects the overlap between the two populations.

C) Bar graph with percentage of Etv1+ defining genes enriched in other epithelial cells.

D) Results from STITCH analysis showing top biological processes and KEGG pathways associated with defining-genes from acinar cells.

Figure 3

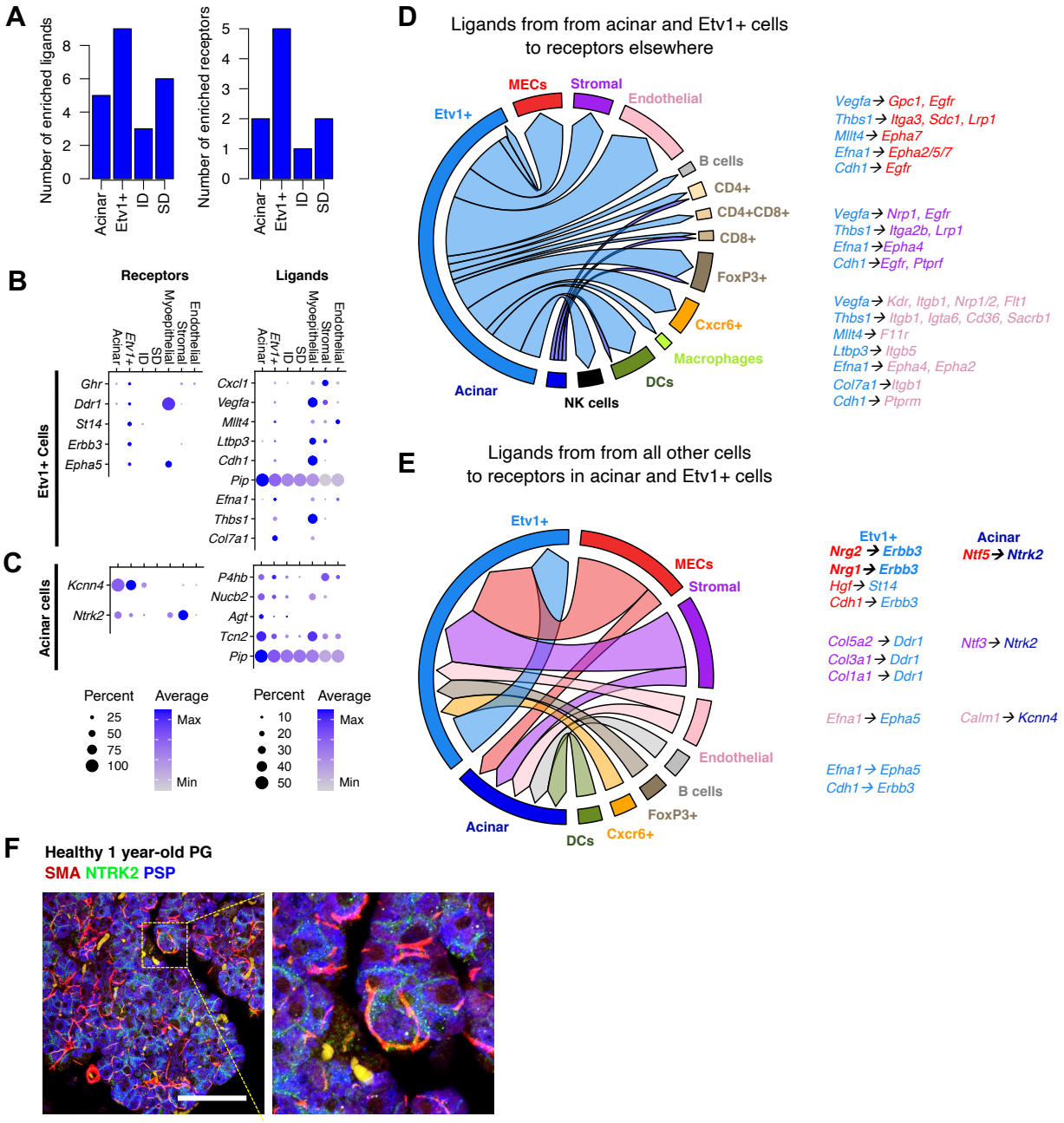

Figure 3. Ligand-receptor analysis of Etv1+ and acinar cells

A) Bar graphs with number of identified ligands and receptors among cell-defining genes from epithelial populations.
B) Balloon plots of expression of ligands and receptors enriched in Etv1+ cells.
C) Balloon plots of expression of ligands and receptors enriched in acinar cells.
D) Chord plot summarizing putative ligand-receptor interactions with Etv1+ cell ligands. The arrows point to the cell expressing the corresponding receptors and are color-coded based on the source of the ligand. The thickness of the arrow is relative to the number of putative pairs identified between Etv1 cells and the cell type pointed by the arrow. Representative ligand-receptor pairs are shown beside the chord plots.
E) Chord plot summarizing putative ligand-receptor interactions with Etv1+ cell receptors.
F) Immunofluorescence staining for Smooth muscle actin (SMA, Red), NTRK2 (green) and Parotid Secretory Protein (PSP, blue). The area delineated by the yellow dotted line is magnified to the right for visualization. Scale bar = 50um.

Supplementary Figure S3, related to Figure 3

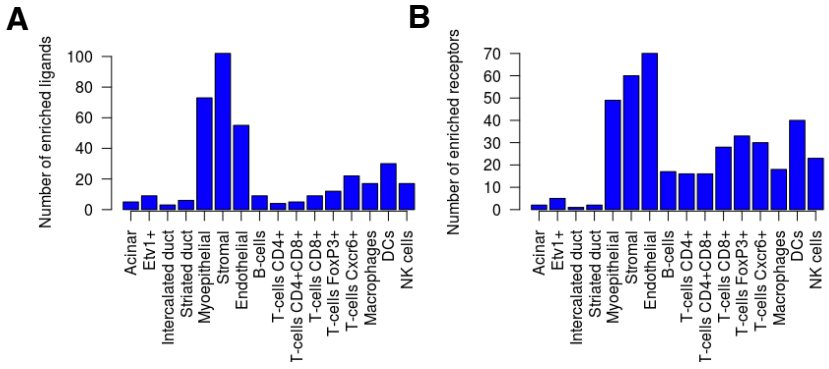

Figure S3. Ligand-receptor analysis of Etv1+ and acinar cells

A-B) Bar graphs with number of identified ligands and receptors among cell-defining genes from all populations.

Table 1:Outgoing ligand-receptor pairs in acinar and Etv1+ cells

From: Acinar		
To	**Number of pairs**	**Pairs**
Acinar	0	
Etv1+	0	
Intercalated duct	0	
Striated duct	0	
Myoepithelial	0	
Stromal	0	
Endothelial	0	
B-cells	0	
T-cells CD4+	1	Pip_cd4
T-cells CD4+CD8+	0	
T-cells CD8+	1	Pip_nptn
T-cells FoxP3+	1	Pip_cd4
T-cells Cxcr6+	0	
Macrophages	0	
DCs	1	Pip_nptn
NK cells	0	

From: Etv1+		
To	**Number of pairs**	**Pairs**
Acinar	0	
Etv1+	2	Efna1_epha5, Cdh1_erbb3
Intercalated duct	0	
Striated duct	0	
Myoepithelial	10	Vegfa_egfr, Vegfa_gpc1, Thbs1_lrp1, Thbs1_sdc1, Thbs1_itga3, Mllt4_epha7, Efna1_epha2, Efna1_epha7, Efna1_epha5, Cdh1_egfr
Stromal	7	Vegfa_nrp1, Vegfa_egfr, Thbs1_itga2b, Thbs1_lrp1, Efna1_epha4, Cdh1_egfr, Cdh1_ptprf
Endothelial	15	Vegfa_kdr, Vegfa_nrp2, Vegfa_itgb1, Vegfa_flt1, Vegfa_nrp1, Thbs1_scarb1, Thbs1_itga6, Thbs1_cd36, Thbs1_itgb1, Mllt4_f11r, Ltbp3_itgb5, Efna1_epha2, Efna1_epha4, Col7a1_itgb1, Cdh1_ptprm
B-cells	2	Thbs1_sdc4, Thbs1_itga4
T-cells CD4+	2	Thbs1_itga6, Pip_cd4
T-cells CD4+CD8+	2	Thbs1_itga6, Cdh1_itgb7
T-cells CD8+	1	Pip_nptn
T-cells FoxP3+	7	Vegfa_itgb1, Thbs1_itgb1, Pip_cd4, Col7a1_itgb1, Cdh1_itgae, Cdh1_igf1r, Cdh1_itgb7
T-cells Cxcr6+	7	Vegfa_ret, Vegfa_itgav, Thbs1_sdc1, Thbs1_itga3, Cdh1_itgae, Cdh1_igf1r, Cdh1_itgb7
Macrophages	2	Vegfa_sirpa, Ltbp3_itgb5
DCs	8	Vegfa_nrp2, Vegfa_itgb1, Thbs1_sdc4, Thbs1_cd47, Thbs1_itga4, Thbs1_itgb1, Pip_nptn, Col7a1_itgb1
NK cells	5	Vegfa_itgb1, Vegfa_gpc1, Thbs1_cd47, Thbs1_itgb1, Col7a1_itgb1

Table 2: Incoming ligand-receptor pairs in acinar and Etv1+ cells

	To acinar		To Etv1+ cells	
From	**Number of pairs**	**Pairs**	**Number of pairs**	**Pairs**
Acinar	0		0	
B-cells	1	Calm1_kcnn4	0	
DCs	1	Calm1_kcnn4	0	
Endothelial	1	Calm1_kcnn4	1	Efna1_epha5
Etv1+	0		2	Efna1_epha5, Cdh1_erbb3
Intercalated duct	0		0	
Macrophages	0		0	
Myoepithelial	1	Ntf5_ntrk2	4	Nrg2_erbb3, Nrg1_erbb3, Hgf_st14, Cdh1_erbb3
NK cells	0		0	
Striated duct	0		0	
Stromal	1	Ntf3_ntrk2	3	Col5a2_ddr1, Col3a1_ddr1, Col1a1_ddr1
T-cells CD4+	0		0	
T-cells CD4+CD8+	0		0	
T-cells CD8+	0		0	
T-cells Cxcr6+	0		1	Areg_erbb3
T-cells FoxP3+	0		1	Areg_erbb3

Figure 4

A

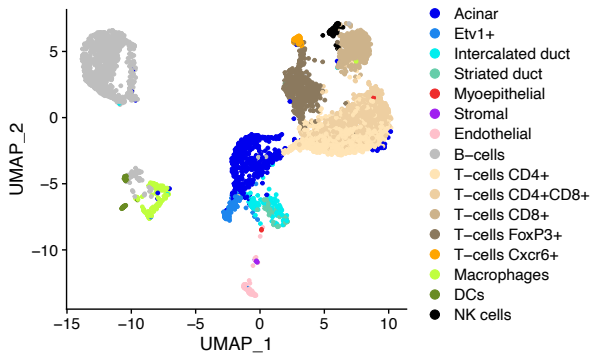

B

	Control		IR	
	Raw	%	Raw	%
Acinar	391	12.6	497	9.8
Etv1+	74	2.4	103	2.0
Intercalated duct	102	3.3	124	2.5
Striated duct	85	2.7	73	1.4
Myoepithelial	4	0.1	6	0.1
Stromal	25	0.8	16	0.3
Endothelial	81	2.6	61	1.2
B-cells	917	29.5	997	19.7
T-cells CD4+	469	15.1	1061	21.0
T-cells CD4+CD8+	275	8.8	871	17.2
T-cells CD8+	223	7.2	403	8.0
T-cells FoxP3+	208	6.7	522	10.3
T-cells Cxcr6+	48	1.5	45	0.9
Macrophages	148	4.8	137	2.7
DCs	37	1.2	68	1.3
NK cells	27	0.9	74	1.5
Total number	3114	100.0	5058	100.0

C

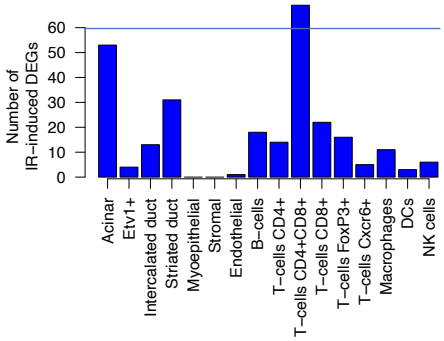

D

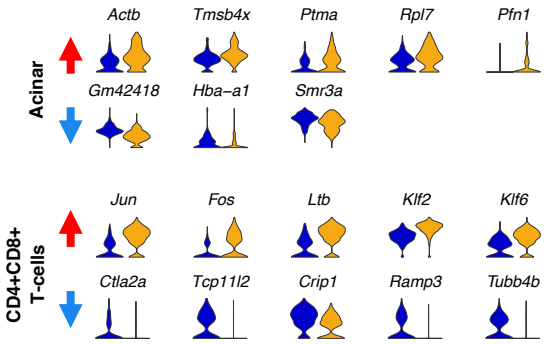

E

GO biological process complete (IR-induced DEGs in acinar cells)	FDR	Genes
regulation of transepithelial transport (GO:0150111)	1.73E-02	Actb, Actg1
electron transport coupled proton transport (GO:0015990)	2.26E-02	mt-Cyb, Mtnd4
energy coupled proton transmembrane transport, against electrochemical gradient (GO:0015988)	2.23E-02	mt-Cyb, Mtnd4
positive regulation of intrinsic apoptotic signaling pathway by p53 class mediator (GO:1902255)	5.35E-04	Ubb, Rpl11, Rps7, Pppia, Rps3, Tpt1, Rack1
regulation of endodeoxyribonuclease activity (GO:0032071)	3.75E-02	Npm1, Rps3
cytoplasmic translation (GO:0002181)	6.15E-15	Rps and Rpl genes
positive regulation of signal transduction by p53 class mediator (GO:1901798)	1.67E-04	Ubb, Rpl11, Rps7, Ddx5

GO biological process complete (IR-induced DEGs in CD4+CD8+ T –cells)	FDR	Genes
T cell receptor V(D)J recombination (GO:0033153)	3.39E-02	Bcl11b, Tcf7
chaperone-mediated protein complex assembly (GO:0051131)	1.45E-02	Hspd1, Hsp90aa1, Hsp90ab1
lymphocyte differentiation (GO:0030098)	5.47E-03	Zfp36l2, Tcf7, Ptpn6, Rhoh, Cd28, Klf6, Gpr183
leukocyte differentiation (GO:0002521)	1.43E-03	Zfp36l2, Tcf7, Junb, Rhoh, Cd28, Klf6, Gpr183, Bcl11b, Jun,
apoptotic signaling pathway (GO:0097190)	3.99E-02	Shisa5, Prkca, Ppp1r15a, Jun, Crip1, Cd28
axonogenesis (GO:0007409)	9.62E-03	Hsp90aa1, Prkca, Emb, Actb, Bcl11b, Evl, Rhoh, Hsp90ab1
regulation of ERK1 and ERK2 cascade (GO:0070372)	4.48E-02	Prkca, Jun, Dusp1, Ptpn6, Gpr183, Ramp3

Figure 4. Cell-specific IR-induced DEGs

A) Representative UMAP of irradiated PG colored by cell type.
B) Cell numbers and proportions in scRNAseq datasets from control and irradiated PG.
C) Bar graph showing number of differentially expressed genes (DEGs) post-IR in individual cell populations. DE analysis was performed with SEURAT's default Wilcoxon test ($p<0.05$).
D) Violin plots of top 5 (if present) up and downregulated genes in acinar and CD4+CD8+ T-cells. Red and blue arrows denote upregulated and downregulated genes, respectively.
E) Representative output from gene ontology analysis with IR-induced DEGs in acinar and CD4+CD8+ T-cells showing dysregulated processes and their associated genes.

Figure S4

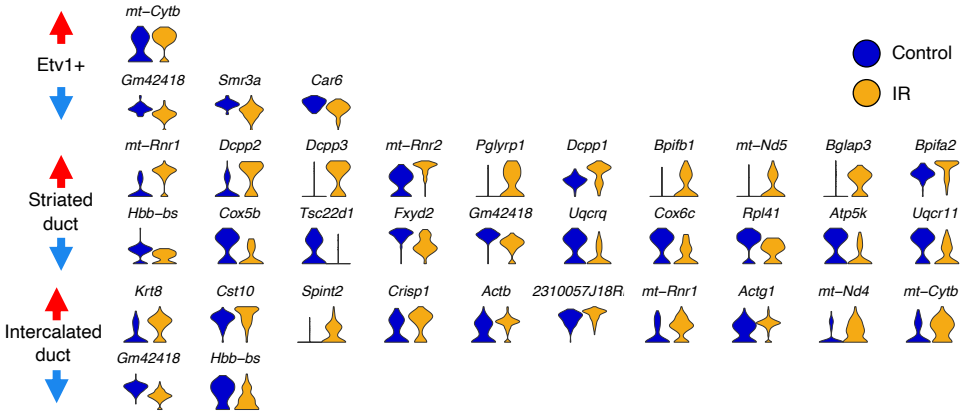

Figure S4. Cell-specific IR-induced DEGs

Violin plots of top 10 (if present) up and downregulated genes in epithelial populations. Red and blue arrows denote upregulated and downregulated genes, respectively.

Figure 5

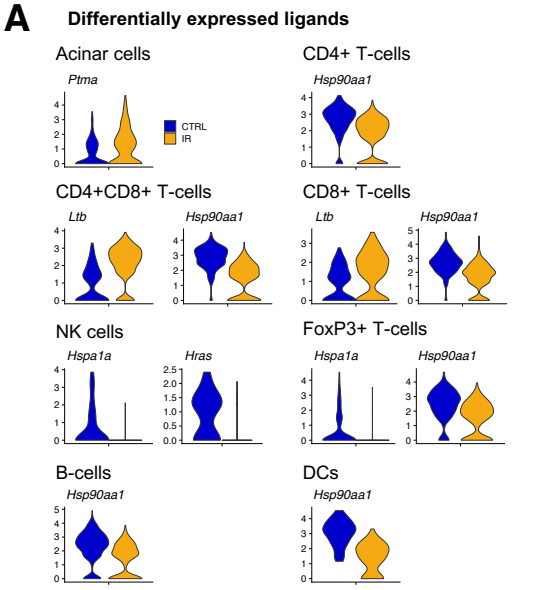

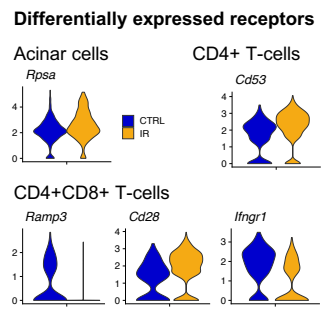

C

Differentially expressed receptors post-IR		
From	**To**	**Pair**
Myoepithelial	Acinar	Lamb2→ Rpsa
Stromal	Acinar	Lama2→ Rpsa, Lamb2→ Rpsa
Endothelial	Acinar	Lamb2→ Rpsa
T-cells CD8+	T-cells CD4+CD8+	Ifng→ Ifngr1
NK cells	T-cells CD4+CD8+	Ifng→ Ifngr1
Differentially expressed ligands post-IR		
From	**To**	**Pair**
B-cells	Myoepithelial	Hsp90aa1→ Egfr
B-cells	Stromal	Hsp90aa1→ Egfr
DCs	Myoepithelial	Hsp90aa1→ Egfr
DCs	Stromal	Hsp90aa1→ Egfr
NK cells	Myoepithelial	Hras→ Sdc2
NK cells	Stromal	Hras→ Sdc2
NK cells	Endothelial	Hras→ Insr, Hras--> Cav1
NK cells	Macrophages	Hras→ Tlr2
T-cells CD4+	Myoepithelial	Hsp90aa1→ Egfr
T-cells CD4+	Stromal	Hsp90aa1→ Egfr
T-cells CD4+CD8+	Myoepithelial	Hsp90aa1→ Egfr
T-cells CD4+CD8+	Stromal	Hsp90aa1→ Egfr, Ltb→ Ltbr, Ltb→ tnfrsf1a
T-cells CD4+CD8+	Endothelial	Ltb→ Tnfrsf1a
T-cells CD4+CD8+	B-cells	Ltb→ Cd40
T-cells CD4+CD8+	Macrophages	Ltb→ Tnfrsf1a
T-cells CD4+CD8+	DCs	Ltb→ Cd40
T-cells CD8+	Myoepithelial	Hsp90aa1→ Egfr
T-cells CD8+	Stromal	Hsp90aa1→ Egfr, Ltb→ Ltbr, Ltb→ tnfrsf1a
T-cells CD8+	Endothelial	Ltb→ Tnfrsf1a
T-cells CD8+	B-cells	Ltb→ Cd40
T-cells CD8+	Macrophages	Ltb→ Tnfrsf1a
T-cells CD8+	DCs	Ltb→ Cd40
T-cells FoxP3+	Myoepithelial	Hsp90aa1→ Egfr
T-cells FoxP3+	Stromal	Hsp90aa1→ Egfr

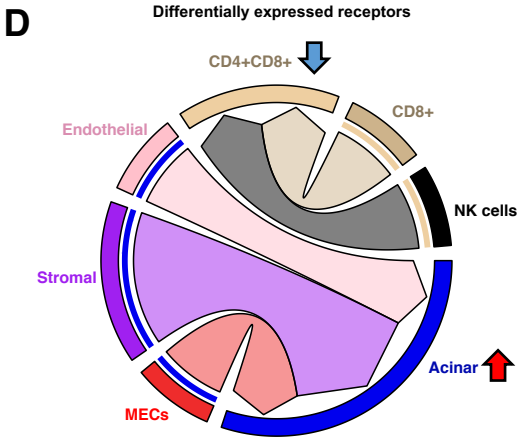

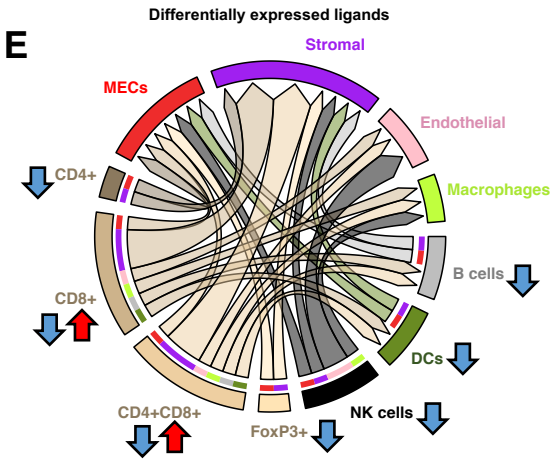

Figure 5. Dysregulated ligand-receptor pairs post-IR

A) Violin plots of differentially expressed receptors.
B) Violin plots of differentially expressed ligands.
C) Chord plot of ligand-receptor interactions with IR-induced DE receptors
D) Chord plot of ligand-receptor interactions with IR-induced DE ligands
E) Summary table with putative ligand-receptor interactions with IR-induced ligands and receptors